Optica Applicata, Vol. LV, No. 3, 2025
DOI: 10.37190/oa/203359

Study of coupling Tamm/Fano resonant states in one-dimensional photonic crystals comprising magnetic fluid for detecting weak magnetic fields

Hussein A. Elsayed[1], Fatma Ramadan[1], Mai Medhat[1], Ahmed M. El-Sherbeeny[2], Wail Al Zoubi[3], Mostafa R. Abukhadra[4,5], Ahmed Mehaney[1,*]

[1]Physics Department, Faculty of Science, Beni-Suef University, Beni-Suef, 62512, Egypt

[2]Industrial Engineering Department, College of Engineering, King Saud University, P.O. Box 800, Riyadh 11421, Saudi Arabia

[3]Materials Electrochemistry Laboratory, School of Materials Science and Engineering, Yeungnam University, Gyeongsan 38541, Republic of Korea

[4]Materials Technologies and their applications Lab, Faculty of Science, Beni-Suef University, Beni Suef city, Egypt

[5]Applied Science Research Center. Applied Science Private University, Amman, Jordan

[*]Corresponding author: ahmed011236@science.bsu.edu.eg

In this research, unconventional coupling of Tamm/Fano states was studied as a magnetic field sensor through a one-dimensional photonic crystal (1D PC) comprising a magnetic fluid. Thus, the magnetic field PC sensor is configured as [prism/Ag/cavity/$(TiO_2/CaF_2)^N$]. In this regard, the cavity layer in this structure is filled with a magnetic fluid of sodium iodide (NaI). This magnetic cavity layer is sandwiched between a thin metallic film of Ag and multilayers of (TiO_2/CaF_2), thereby allowing this sensor to be very sensitive to any change in the applied magnetic field. The reflectance spectrum is analyzed based on the fundamentals of the transfer matrix method (TMM). In addition, all sensor parameters have been optimized to get the optimal conditions for the sensor performance. Moreover, numerical results showed that changing the intensity of the external applied magnetic field has a significant effect on the refractive index of the magnetic fluid and observed significant shifts in the position of the localized Tamm/Fano modes. Finally, different performance parameters are calculated, among them, a superb sensitivity is obtained with the value of 1500 nm/RIU at a magnetic field of just 50 Oe, which recommends this magnetic sensor as a good candidate in numerous magnetic applications.

Keywords: photonic crystal magnetic field sensor, cavity layer, magnetic fluid, Tamm plasmon resonance, Fano resonance.

1. Introduction

In 1987, YABLONOVITCH [1] and JOHN [2] have proposed a new kind of artificial periodic materials known as photonic crystals (PCs). Meanwhile, PCs have played pioneering role in many applications in the last three decades due to their unique properties. PCs are man-made structures with different refractive indices arranged periodically in 1D, 2D or 3D [3-5]. PCs are characterized by the so-called photonic band gaps (PBGs) and photon localization modes. The emergence of these PBGs provides a promising role in controlling the propagation of electromagnetic waves (EMWs) in 1D, 2D or 3D. Meanwhile, the appearance of these bands through 3D structures could provide the ability to completely inhibit spontaneous emission and localize the light [3-6]. Consequently, photon localization provides discontinuous electromagnetic waves in the PBG due to breaking the periodicity of the periodic structure by defects or cavities [7]. Interestingly, PCs have received a considerable effect in many applications such as reflectors [8-14], resonators [15], optical resonators [16], optical filters [17], gas sensors [18,19], temperature sensors [20,21], magnetic field sensors [22] and water desalination applications [23].

Nowadays, the phenomenon of Tamm plasmon resonances (TPR) is demonstrated in PC designs for many sensing applications. This phenomenon appears at the interface between a metallic layer and dielectric designs of PCs due to localized surface plasmon polariton [24,25]. While the surface plasmon polariton [26] is a surface wave which propagates along the interface between metal and dielectric, this wave is formed by the collective motion of electrons in the metal. Meanwhile, the collective motion provides a localized oscillation via the propagating of EMWs which are confined to the interface. Moreover, TPR is characterized by a sharp resonant peak in the transmittance or reflectance of the spectrum of the PC structure. In addition, the excitation of TPR with EMWs, the shift in reflectivity spectra is observed. Notably, TPR demonstrates high sensitivity and high-quality factor in the optical sensing [24,27].

Otherwise, another phenomenon that is illustrated in PC structures is known as Fano resonance [28,29]. Up to now, Fano resonance is a state of resonance, which is established from theoretical aspects and explanations by Ugo Fano in 1961. As long as, Fano resonance appears as an asymmetric line shape in the transmission and reflection spectrum of the PCs framework. As well, the appearance of Fano resonance is due to the interference between the resonance mode with the continuum of radiation modes which behaves as a broad background spectrum. Consequently, if this interference is constructive it leads to a peak in the transmission or reflection spectrum, while the destructive interference leads to a dip or anti-resonance. Over and above, Fano resonance has a wide range of applications such as electro-optical applications and chemical or biological sensing [30,31].

Posteriorly, when a magnetic field interacts with PCs, it causes significant changes in the permittivity of metals, semiconductors, and used materials. These changes in the permittivity of these materials are due to the magneto-optic effects [32,33]. Thus, the magneto-optical influences are classified to two effects, the Faraday effect, and the

Voigt effect [32,33]. The direction of the applied magnetic field is normal to the direction of the propagation of EMWs in Faraday effect, while, in Voigt effect it is parallel to the direction of the propagation of EMWs. Moreover, both effects are certainly related to the interaction of EMWs with the component materials of the structure.

Herein, we intend to study the characteristics of a magnetic field sensor based on our unique PC design, which displays Tamm/Fano plasmon resonance inside the PBG by using a magnetic fluid inside a defect layer [34]. Magnetic fluid is a liquid magnetic material, which has high sensitivity to magnetic effect and the ability to change its refractive index and optical properties via the exposure to the external magnetic field. Thus, this effect will lead to changes in the PBG properties and localized modes as well. Therefore, the presence of external magnetic field affects the magnetic nanoparticles of the magnetic fluid by aligning it with the field orientation [34,35]. Besides the changes on the refractive index of the magnetic fluid, the PBG and position of produced Tamm/Fano modes will be shifted. In the beginning, we will carry out a comprehensive optimization process on all the sensor parameters to set up the optimal PC magnetic field sensor design. In what follows, we will focus on the production of Tamm/Fano modes through this material and show how the PBGs can be affected with the applied magnetic field and discuss the performance of the sensor according to many parameters. Finally, we will highlight the suitable application of our candidate design according to the finding results as will be discussed in the next sections.

2. Structure design

In this work, we present the essential design of the 1D PCs in which each unit cell is composed of two layers of titanium dioxide and calcium fluoride (TiO_2 and CaF_2), with thicknesses $d_1 = 100$ nm and $d_2 = 600$ nm, respectively. In this regard, the designed structure provides a periodicity number N of 15 repeated unit cells. Then, a cavity layer of thickness $d_c = 5$ μm is deposited over the designed PC structure. This cavity layer is filled of the analyte material, sodium iodide (NaI). In addition, a thin metallic layer of sliver (Ag) layer with thickness $d_m = 30$ nm is introduced over the cavity layer to generate the resonant peak inside the PBG. Finally, we use a prism, which is located

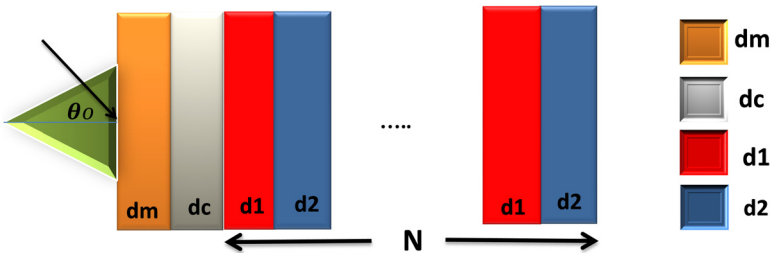

Fig. 1. The schematic diagram of the 1D PC structure consisting of metallic layer on the top surface, then a cavity layer d_c of NaI beside periodic dielectric materials of TiO_2 and CaF_2 are repeated N times. Also, the prism is in located in the front of the whole structure to allow the best interaction between EMW's and the applied magnetic field.

in front of the face of Ag layer. As well, our final designed structure is configured as [prism/Ag/ cavity/$(TiO_2/CaF_2)^{15}$] as mentioned in Fig. 1.

3. TMM formulization

Here, our sensor could be analyzed through a unique theoretical method. Specifically, after inserting the NaI into the cavity inside the PC design where it is situated between the metallic layer of Ag and TiO_2/CaF_2 multilayers. Thus, this layer of NaI illustrates distinguishable optical characteristics via the interaction with EMWs and applied magnetic field. In addition, the metallic layer is located on the top of the PC that is necessary for appearing the Tamm/Fano resonance inside the resultant PBG. In the following, unless mentioned otherwise, the incident angle of light on the proposed structure has fixed value approximately $\theta_0 = 20°$. Notably, the whole schematic of the sensor will be arranged as [prism/Ag/ cavity/$(TiO_2/CaF_2)^N$], where N refers to the periodicity of the PC structure.

Now, according to the characteristic formalism, which is known as the transfer matrix method (TMM), we can manifest the theoretical fundamentals of the proposed design and optical parameters of the sensor [36-38]. According to this method, the magnetic and electric components of EMWs will be considered in the Z-direction. The amplitudes of the electric E_j and magnetic H_j in a layer j are given as follows:

$$E_j(z) = G_j \exp(-i k_j z) + H_j \exp(-i k_j z) = E_{y+} + E_{y-} \tag{1}$$

$$\begin{aligned} H_j(z) &= \frac{-i}{\omega}\frac{\partial E}{\partial z} = \frac{-k_j}{\omega}\left[-G_j \exp(-i k_j z) + H_j \exp(-i k_j z)\right] \\ &= \frac{k_j}{\omega}(E_{y+} + E_{y-}) = \Gamma(E_{y+} - E_{y-}) \end{aligned} \tag{2}$$

where $k_j = k_0 n_j \cos(\theta_j)$, and G, H are two constants, n is the refractive index, and θ_j is the incident angle. Then, the electric and magnetic components can be described as follows:

$$\begin{bmatrix} E_j(z) \\ H_j(z) \end{bmatrix} = \begin{bmatrix} 1 & 1 \\ p_j & -p_j \end{bmatrix} \begin{bmatrix} E_{y+} \\ E_{y-} \end{bmatrix}, \quad \begin{bmatrix} E_{y+} \\ E_{y-} \end{bmatrix} = \frac{1}{2} \begin{bmatrix} 1 & 1/p_j \\ 1 & -1/p_j \end{bmatrix} \begin{bmatrix} E_j(z) \\ H_j(z) \end{bmatrix} \tag{3}$$

By reformulated Eqs. (1) and (3) we get:

$$\begin{bmatrix} E_{y1+} \\ E_{y1-} \end{bmatrix} = \begin{bmatrix} \exp(i\beta_j) & 0 \\ 0 & \exp(-i\beta_j) \end{bmatrix} \begin{bmatrix} E_{y2+} \\ E_{y2-} \end{bmatrix} \tag{4}$$

where $\beta_j = k_j d_j$, and k_j refers to the wave vector, d_j is the thickness of each layer. This can happen when the incident waves interact with a featured layer having the thickness of $d_j = Z_2 - Z_1$.

From Eqs. (3) and (4):

$$\begin{bmatrix} E_1(z) \\ H_1(z) \end{bmatrix} = \begin{bmatrix} 1 & 1 \\ p_j & -p_j \end{bmatrix} \begin{bmatrix} E_{y1+} \\ E_{y1-} \end{bmatrix}$$

$$= \begin{bmatrix} 1 & 1 \\ p_j & -p_j \end{bmatrix} \begin{bmatrix} \exp(i\beta_j) & 0 \\ 0 & \exp(-i\beta_j) \end{bmatrix} \begin{bmatrix} E_{y2+} \\ E_{y2-} \end{bmatrix}$$

$$= \frac{1}{2} \begin{bmatrix} 1 & 1 \\ p_j & -p_j \end{bmatrix} \begin{bmatrix} \exp(i\beta_j) & 0 \\ 0 & \exp(-i\beta_j) \end{bmatrix} \begin{bmatrix} 1 & 1/p_j \\ 1 & -1/p_j \end{bmatrix} \begin{bmatrix} E_2(z) \\ H_2(z) \end{bmatrix}$$

$$= \begin{bmatrix} \cos\beta_j & \dfrac{-i\sin\beta_j}{p_j} \\ -ip_j \sin\beta_j & \cos\beta_j \end{bmatrix} \begin{bmatrix} E_2(z) \\ H_2(z) \end{bmatrix} = f_j \begin{bmatrix} E_2(z) \\ H_2(z) \end{bmatrix} \tag{5}$$

where f_j expresses the relation between the electric and magnetic fields components along the layer j. Consequently, the total characteristic matrix for the full structure layers which interact with the incident electromagnetic waves can be described as follows:

$$F = \begin{bmatrix} F_{11} & F_{12} \\ F_{21} & F_{22} \end{bmatrix} = \prod_{j=1}^{k} F_j \tag{6}$$

where F_{11}, F_{12}, F_{21}, and F_{22} are the matrices of the total structure. Finally, the reflectance of the incident electromagnetic waves is given by:

$$r = \left| \frac{(F_{11}P_o + F_{12}P_sP_o) - (F_{21} + F_{22}P_o)}{(F_{11}P_o + F_{12}P_sP_o) + (F_{21} + F_{22}P_s)} \right|, \qquad R = r^2 \tag{7}$$

Here P_o stands for the prism and P_s represents the substrate. These two coefficients are given by: $P_o = n_o \cos\theta_o$ and $P_s = n_s \cos\theta_s$. Now, the EMWs interact with 1D defective PCs by applying the external magnetic field H. On the other hand, the permittivity of the Ag layer can be determined from the Drude model formula, and it is given by [38]:

$$\varepsilon = 1 - \frac{\omega_p^2}{\omega^2 + i\gamma\omega} \tag{8}$$

where ω is the frequency of the incident radiation rays ($\omega = 2\pi c/\lambda$), c is the speed of light. Here, ω_p is the plasmon frequency of the Ag layer $\omega_p = 13.69 \times 10^{15}$ rad/sec,

while γ is the Ag damping constant that approaches to $\gamma = 27.35 \times 10^{12}$ rad/sec [38]. Then, the refractive index of the metallic layer of Ag could be calculated from

$$n_{\mathrm{m}} = \sqrt{\varepsilon} \tag{9}$$

Moreover, the refractive index of the magnetic fluid is an essential parameter for optical sensing applications. Therefore, it is necessary to get the refractive index as a function of applied magnetic field. The refractive index of the magnetic fluid could be computed by the Langevin function [39] as follows:

$$n_{\mathrm{c}} = (n_{\mathrm{s}} - n_{\mathrm{o}}) \left\{ \coth \left[\frac{\varphi (H - H_{\mathrm{c}})}{T} \right] - \frac{T}{\alpha (H - H_{\mathrm{c}})} \right\} + n_{\mathrm{o}} \tag{10}$$

where, H is the magnetic field strength in Oe, $H_{\mathrm{c,n}}$ is the magnetic field strength that is related to liquid and concentration of the magnetic field, n_{s} is the saturated refractive index and n_{o} is the initial refractive index of magnetic fluid. Here, φ describes the fitting parameter, and T is the operating temperature.

4. Results and discussion

4.1. Optimization of sensor parameters

In this section, we will present our magnetic sensor in the configuration of (metallic layer/NaI cavity layer/dielectric multilayers). So that, we will pursue in elucidation the dominant parameters which have significant effects on the efficiency and optical properties of the sensor. For instance, the type of metal, components of dielectric multilayers, and thickness of each layer. Besides these factors, we will study the impact of periodicity parameter and variation of incident angle on the sensor performance as well. Therefore, we fluctuate the intensity of applied magnetic field value at two different values of the previous parameters. Moreover, we will repeat the last step for each design parameters and calculate the sensitivity of the sensor until reach the optimal and best conditions.

4.2. Optimization of the type of the first layer

Here, we intend to find the best material used as a first layer in the PC based on its effect on the sensitivity of our sensor. Therefore, we firstly set our first candidate materials of the structure as (Ag metal layer/NaI cavity layer/Al_2O_3/CaF_2) with the number of periodicity of PC, $N = 15$. Now, we alternate between aluminum dioxide Al_2O_3, yttrium (III) oxide Y_2O_3 and titanium dioxide TiO_2 as the first layer of our structure by keeping the other parameters without changing. Also, we would change the intensity of the magnetic field and determine the sensitivity of our sensor. Firstly, without any applied magnetic field and secondly, when the intensity of magnetic field equals 100 Oe as seen in Fig. 2. We achieve the highest sensitivity when using titanium dioxide TiO_2 as the first layer of PC. Where, the maximum sensitivity is about 1100 nm/RIU, and

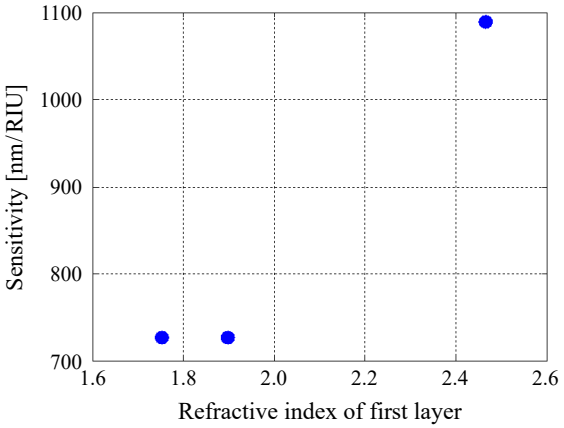

Fig. 2. The sensitivity of our sensor when magnetic field intensities have values between 0 and 100 Oe with different materials of the first dielectric layer (such as Al_2O_3, Y_2O_3, and TiO_2).

other materials do not exceed 750 nm/RIU. So, the sensor structure becomes firstly as [Ag metal layer/NaI cavity layer/$(TiO_2/CaF_2)^{15}$].

4.3. Optimization of the second layer

On the other hand, the second step of optimization is the second layer of the dielectric stack in our sensor in examining different materials (such as MgF_2, Al_2O_3, SiO_2, Y_2O_3, and CaF_2). The thicknesses of each layer in our structure is not changed until now. We also applied different magnetic field intensities on the structure between 0 and 100 Oe and calculated the sensitivity of structure while changing the second layer of this PC. According to these different materials (MgF_2, Al_2O_3, SiO_2, Y_2O_3, CaF_2) with refractive indices n_2 in the PC. As can be seen in Fig. 3, the sensitivity reaches the highest value

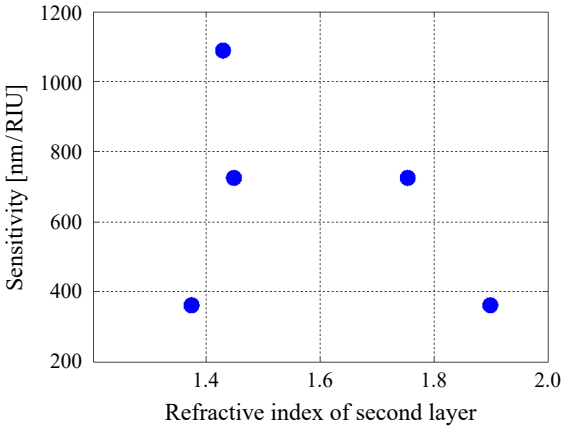

Fig. 3. The sensor sensitivity against the refractive indices of different materials of the second layer (such as MgF_2, Al_2O_3, SiO_2, Y_2O_3, and CaF_2) at different magnetic field intensities.

which approach to the value of 1100 nm/RIU, when using calcium fluoride CaF_2. Therefore, the structure of sensor now reaches the configuration of [Ag metal/cavity layer (NaI)/$(TiO_2/CaF_2)^{15}$].

4.4. Optimization of the type of metallic layer

Now, we will optimize the effect of the metallic layer on the sensor sensitivity. The configuration [Ag metal/cavity layer (NaI)/$(TiO_2/CaF_2)^{15}$] has the same previous mentioned thicknesses at condition of applying magnetic fields by 0 and 100 Oe, while, changing the type of used metal in our structure. These metallic materials such as silver, gold, aluminum, and even platinum illustrate unique responses based on their real and imaginary part of permittivity through interaction with EMWs. In Fig. 4, the highest sensitivity of our design reaches to more than 1400 nm/RIU when using Ag rather than other metals due to its low optical losses and the lowest attenuation part [37,38]. To sum up, the dependence on Ag, TiO_2 and CaF_2 layers in the design of the proposed sensor represents the best choice towards the best performance. Notably, the inclusion of TiO_2 and CaF_2 through each unit cell of our PC structure gives rise to the best sensitivity as depicted in Figs. 2 and 3. Moreover, these two materials provide a relatively high contrast between their indices of refraction, which, in turns, leads to a relatively wide PBG compared with other pairs. This strategy could be of a significant interest towards a smooth and simple shift of the introduced resonant peak whatever the intensity of the applied external magnetic field. In contrast, the inclusion of Ag metal could be promising towards high sensitivity and high-quality factor as well of the designed sensor compared with other metals as demonstrated in Fig. 4. Notably, Ag provides low optical losses due to its small damping value [38]. Therefore, the full width at half maximum of the emerged peak is expected to be small which in turns could

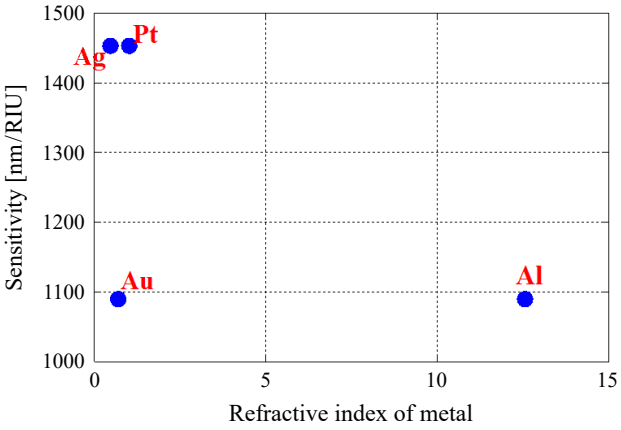

Fig. 4. The sensitivity of the proposed sensor with different metallic materials (such as Al, Au, Ag, Pt) at different intensities of magnetic field (0 and 100 Oe).

give rise to the best quality factor value. So that, the structure now is configured as on [Ag metal/cavity layer (NaI)/$(TiO_2/CaF_2)^{15}$].

4.5. Optimization of the thickness of each layer

Firstly, we aim to identify the optimal thickness of the first layer of the dielectric multilayers in the photonic crystal (PC) structure that yields the highest sensitivity in both the absence and presence of the applied magnetic field, specifically at 0 and 100 Oe. For these two magnetic field intensities, we evaluate the sensitivity of our sensor at various thicknesses of the first layer. Consequently, we utilize different thicknesses of titanium dioxide for this analysis d_1 = 40, 80, 100 and 120 nm. In this regard, the increase in the thickness of the first dielectric layer led to inflation in the sensitivity from 720 to 1100 nm/RIU as shown in Fig. 5. Although, the elevation in the sensitivity with increasing the thickness of TiO_2, the continuous increasing in d_1 over 100 nm led to drop down in the value of this sensitivity to reach about below the value of 750 nm/Oe.

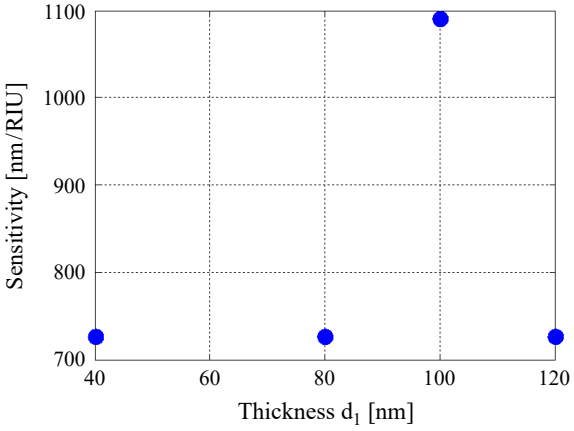

Fig. 5. The sensitivity of the proposed sensor at different thicknesses of the first layer (TiO_2) (40, 80, 100, and 120 nm) for two intensities of the magnetic field (0 and 100 Oe).

Then, Fig. 6 demonstrates a brilliant effect of the second layer CaF_2 thickness on the sensitivity value of the sensor at specific values such as 300, 600, 900, 1200, and 1500 nm. While the variation in applied magnetic field values between 0 and 100 Oe, the sensitivity increases gradually between 0.02 and 0.04 nm/RIU. Thus, the maximum sensitivity occurs when the thickness of the second layer equals d_2 = 600 nm as seen in Fig. 6.

Next, as illustrated in Fig. 7, the sensitivity will be in augmentation with outgrowth in the thickness of the thin metallic film, until achieving stability in the sensitivity value of about 1500 nm/RIU between 20 and 30 nm thickness, Also, the sensitivity is decreasing with continuous accretion of Ag thickness. Therefore, the highest sensitivity

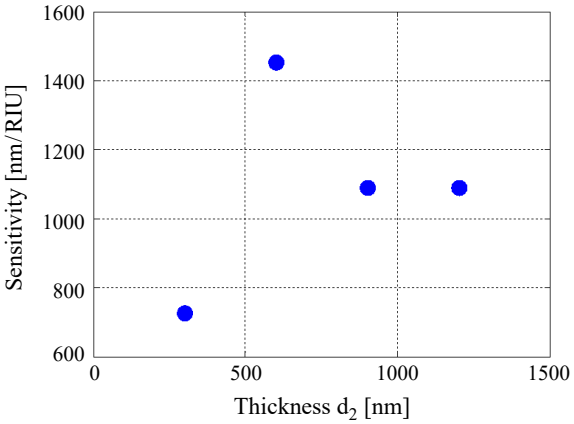

Fig. 6. The sensitivity when using different thicknesses of the second layer (CaF_2) (300, 600, 900, and 1200 nm) under the effect of magnetic field (0 and 100 Oe).

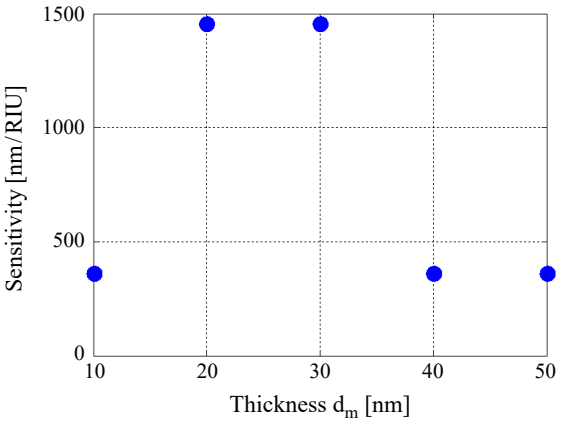

Fig. 7. The sensitivity of the sensor at different thicknesses of the metal layer (Ag) (10, 20, 30, 40, and 50 nm) under the effect of the magnetic field (0 and 100 Oe).

occurs when the thickness of the metal layer is d_m = 20 nm and d_m = 30 nm as seen in Fig. 7. From this optimization, we choose the thickness of Ag layer d_m = 30 nm because it gives the highest sensitivity, and it will be more suitable to produce the coupling between Fano and Tamm resonances through the PBG.

Finally, the cavity of the structure is situated between the metal and dielectric multilayers, making its position crucial as it underpins our sensing mechanism. This cavity layer is filled with sodium iodide (NaI), which exhibits heightened sensitivity to changes in the applied magnetic field. The variation in the refractive index of the NaI medium due to the magnetic field is responsible for the emergence of the Tamm plasmonic resonance (TPR) state; thus, any alteration in the cavity region will affect the TPR mode. The maximum sensitivity of 1450 nm/RIU occurs at a cavity layer

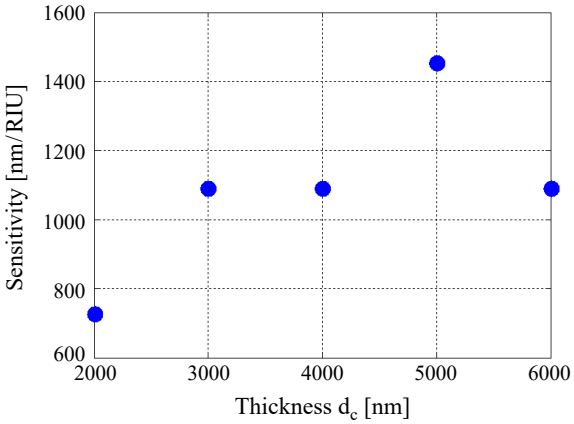

Fig. 8. The sensitivity at different thicknesses of the cavity layer (NaI) (2000, 3000, 4000, 5000, and 6000 nm) at different intensities of the magnetic field exposure (0 and 100 Oe).

thickness of d_c = 5000 nm, as illustrated in Fig. 8. It is essential for the cavity layer to be of substantial size to enhance the interaction between the slow mode (plasmonic mode in the metal) and the broad band of the photonic crystal (PC), which facilitates the simultaneous generation of Fano modes coupled with the Tamm mode [36-38].

4.6. Optimization of the periodicity number

In this subsection, we examine the effect of the number of periods on the sensitivity of the sensor while varying the intensity of the magnetic field (0 and 100 Oe). We adjusted the number of periods from N = 5 to N = 20 and assessed the sensitivity at each value to identify which periodicity yields the best performance. As shown in Fig. 9, we found that N = 15 provides the highest sensitivity at 1500 nm/RIU. Additionally,

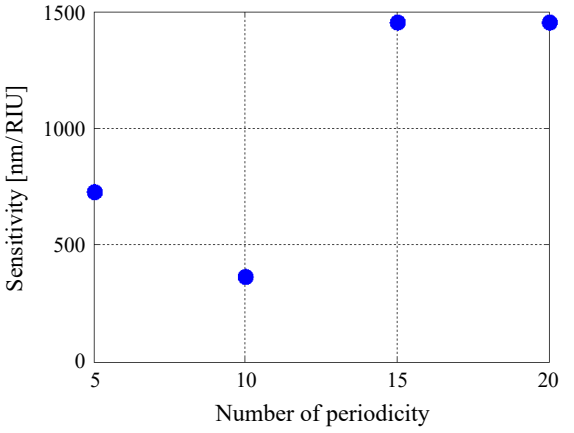

Fig. 9. The effect of the number of periodicity on the sensitivity of the PC structure at 0 and 100 Oe.

we observed that a periodicity of 20 also achieves the same maximum sensitivity. However, we opted for the lower value, $N = 15$, to minimize the number of periods from a cost perspective.

4.7. Optimization of the incident angle

Lastly, we vary the incident angle from $\theta_0 = 0°$ to $\theta_0 = 25°$. At these angles, we assess the sensitivity of the sensor under both zero magnetic field and 100 Oe. As shown in Fig. 10, the incident angle θ_0 that yields the maximum sensitivity is 20°. When the incident angle is increased from normal incidence to 20°, the sensitivity changes from 1480 to over 1510 nm/RIU. It is important to note that increasing the incident angle enhances total reflection through the prism, which improves the formation of Tamm/Fano modes with high sharpness and facilitates their displacement in response to the magnetic field [38,39]. Beyond the angle of 20°, the total reelection increases to the extent to preventing any resonant peak from appearing inside the PBGs.

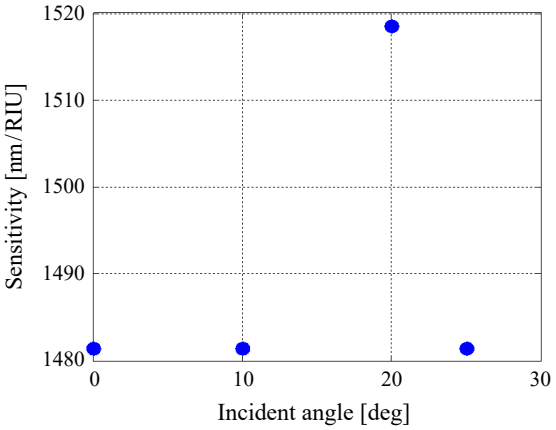

Fig. 10. The sensitivity of our sensor at different incident angles.

Using the analysis stated above, we reached now to the final optimal sensor structure that gives the highest sensitivity. The structure of the sensor is configurated as [Ag metal/cavity layer (NaI)/$(TiO_2/CaF_2)^{15}$], where the thicknesses of the sensor's layers are $d_1 = 100$ nm, $d_2 = 600$ nm, $d_m = 30$ nm and $d_c = 5000$ nm. The incident angle is taken as $\theta_0 = 20°$.

4.8. The reflectance spectrum of our designed sensor

In this context, the effective refractive index of the magnetic fluid (NaI) depends on the applied magnetic field and temperature. So that, the refractive index of magnetic fluid can be calculated by the Langevin function as shown in Eq. (10). Here, the parameters of this relation are $n_b = 1.4620$, $H_{c,n} = 30$ Oe, $n_s = 1.4704$, $\varphi = 3$, and $T = 298$ K.

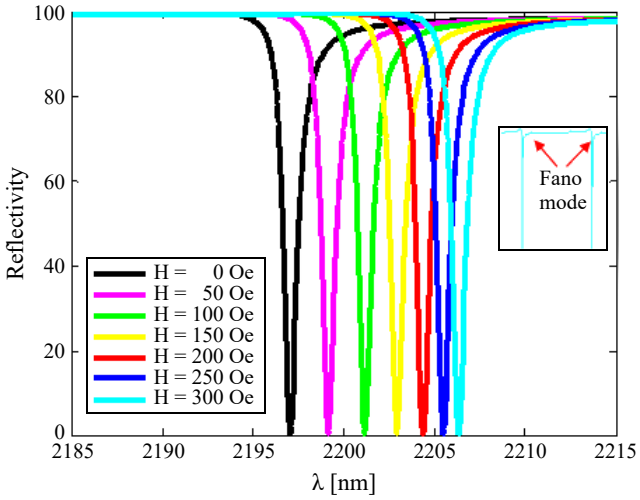

Fig. 11. The reflectance spectrum of our designed sensor at different intensities of the applied magnetic field from 0 to 300 Oe.

Figure 11 illustrates the impact of the external magnetic field on the position of the TP/Fano resonance mode. As the external magnetic field increases to 50 Oe, the TP resonance peak shifts upward from 2197 to 2199.1 nm. Moreover, as the magnetic field strength rises to 100, 150, 200, 250, and 300 Oe, the resonant peak shifts to 2201.1, 2203, 2204.4, 2205.5, and 2206.2 nm, respectively. Additionally, with the increase in the applied magnetic field, the resonance states shift toward higher wavelengths while maintaining the same intensity of the resonance peak.

To sum up, Fig. 12 shows the dependence of the TP position on the intensity of the applied magnetic field. The fitting figure shows that the wavelength of TP/Fano res-

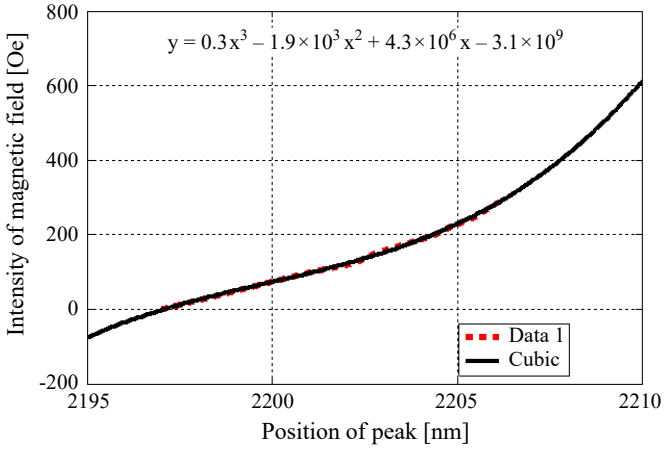

Fig. 12. The dependence of the TP position on the intensity of the applied magnetic field.

onance varies with intensity of the applied magnetic field. This response is demonstrated according to the following relation:

$$H(\mathrm{Oe}) = 0.3\,\lambda_{\mathrm{res}}^{3} - 1.9 \times 10^{3}\,\lambda_{\mathrm{res}}^{2} + 4.3 \times 10^{6}\,\lambda_{\mathrm{res}} - 3.1 \times 10^{9} \tag{11}$$

According to this relation, the intensity of the magnetic field can be obtained with high accuracy and clarity based on the wavelength values of the TP resonance peak.

4.9. The sensor performance

In this section, we discuss and calculate the sensor performance with changing the applied magnetic field. The performance of the sensor is controlled by many parameters. Here, we calculate the sensitivity (S), full width at high maximum (FWHM), the signal to noise ratio (SNR), the quality factor (QF), the figure of merit (FOM), the detection limit (DL), and the sensor resolution (SR). These factors are given as follows:

$$S = \frac{\Delta\lambda_{\mathrm{res}}}{\Delta H} \tag{12}$$

$$S = \frac{\Delta\lambda_{\mathrm{res}}}{\Delta n} \tag{13}$$

$$\mathrm{QF} = \frac{\lambda_{\mathrm{res}}}{\mathrm{FWHM}} \tag{14}$$

$$\mathrm{SNR} = \frac{\Delta\lambda_{\mathrm{res}}}{\mathrm{FWHM}} \tag{15}$$

$$\mathrm{DL} = \frac{2}{5}\,\frac{\mathrm{FWHM}}{3(\mathrm{SNR})^{0.25}} \tag{16}$$

$$\mathrm{SR} = \mathrm{DL} \times S \tag{17}$$

$$\mathrm{FOM} = \frac{S}{\mathrm{FWHM}} \tag{18}$$

where FWHM is the full width at half maximum of the dip value, and λ_{res} is the Tamm/Fano dip wavelength value. Table 1 illustrates these parameters.

4.9.1. Discussion of the performance of the PC magnetic sensor under changing the applied magnetic field

As illustrated in Eq. (11), changing the intensity of the applied magnetic field alters the position λ_{res} of Tamm/Fano mode. So that, we notice that any increase in the intensity of the applied magnetic field more than 50 Oe led to a decrease in the sensitivity value until reaching the value of 7.35 nm/Oe as seen in Table 1. In addition, the re-

T a b l e 1. The performance parameters of the PC magnetic sensor.

H [Oe]	λ_{res} [nm]	FWHM	QF	S [nm/Oe]	SNR	DL [Oe]	SR	FOM [nm^{-1}]	S [nm/RIU]
0	2197	0.5	4394						
50	2199.1	1.1	1999.2	43.982	1.91	0.014	0.62	39.98	1500
100	2201.1	0.9	2445.7	22.011	4.56	0.019	0.42	24.46	1518.52
150	2203	0.9	2447.8	14.687	6.67	0.025	0.37	16.32	1538.46
200	2204.4	0.9	2449.3	11.022	8.22	0.032	0.35	12.25	1510.2
250	2205.5	0.9	2450.6	8.822	9.44	0.039	0.34	9.8	1517.86
300	2206.6	0.9	2451.3	7.354	10.2	0.046	0.338	8.17	1548.38

T a b l e 2. The values of the refractive index of the cavity layer *versus* the magnetic field.

H [Oe]	n [RIU]	Δn [RIU]
0	1.4612	0
50	1.4626	0.0014
100	1.4639	0.0027
150	1.4651	0.0039
200	1.4661	0.0049
250	1.4668	0.0056
300	1.4674	0.0062

fractive index of the cavity layer will alter due to the change in the intensity of the applied magnetic field. Moreover, we found that the respond in risingthe intensity of magnetic field appears through the slight accretion of the refractive index of the cavity medium as shown in Table 2. Meanwhile, the cavity medium of NaI that is used in our magnetic sensor is considered as a sensitive ambience to any alteration in the external magnetic field.

Now, we discuss a brief summary of the sensor parameters and sensitivity in nm/Oe and nm/RIU as seen in Fig. 13. However, after the brilliant increase in sensitivity that reached up to 1500 nm/RIU, the sensitivity decreases gradually with increasing applied magnetic field until the value less than 10 nm/Oe. Then, Fig. 13(b) manifests the growing in the FWHM from 0.5 to 0.9 nm and achieves the stability at the highest value of the magnetic field. So that, the quality factor (QF) records the maximum value of about 4394 which means this PC magnetic sensor introduces higher performance and efficiency. In addition to this value, the stability of QF enhances the accuracy of measurements and makes it suitable for many applications where accurate results are required. In this regard, we noticed that FOM and SNR decrease when the magnetic field increases from 0 to 300 Oe as shown in Fig. 13(c). This increase of SNR enhances the sensor's sensitivity and allows more reliable detection of small changes in the magnetic field even if there is a noise or electromagnetic interference. Moreover, Fig. 13(d) demonstrates the increment in DL and decrement in the sensor resolution (SR) under

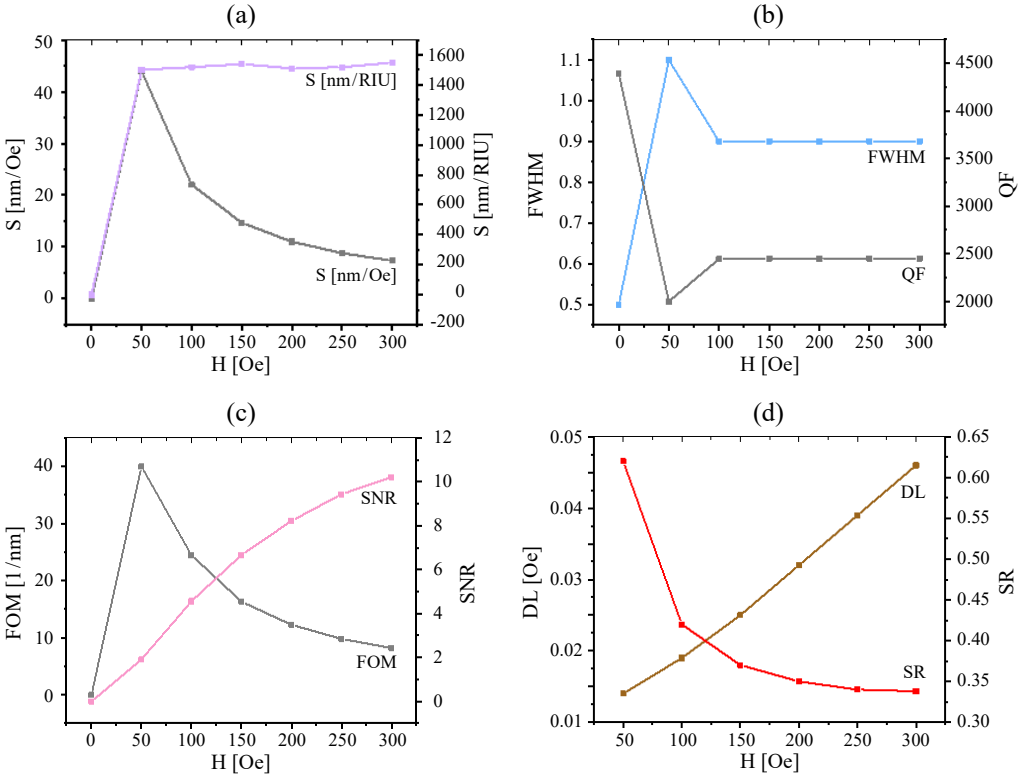

Fig. 13. The performance factors of the proposed PC magnetic sensor with changing the magnetic field.

the variation of magnetic field values. Surely, the minimum value of DL as 0.015 Oe ensures the high efficacy of this detector.

Finally, there are some environmental conditions that could lead to some effects on the performance of this designed sensor. In this regard, temperature fluctuations, mechanical stress and humidity as well could provide some effects on the performance of the suggested magnetic fluid sensor due to the changes in the indices of refraction with these parameters. However, the considered materials provide small values for their thermo-optic coefficients which in turn could give rise to limited changes in the performance of the designed sensor due to the limited shift in the position of the coupled Tamm/Fano resonance with the temperature variations. Meanwhile, we believe that this limited shift can be controlled or corrected using some algorithms for temperature compensation based on the machine learning technique. In contrast, the surface of the designed sensor may suffer from an increased level of the absorbed water with the increments in humidity levels. This effect could lead to significant changes in the performance and efficiency of the sensor over the long time. Therefore, we believe that a thin protective hydrophobic layer of SiO_2 or Al_2O_3 can be introduced for encapsulating the designed sensor to mitigate this effect. Then, to overcome the neg-

ative effects of the mechanical stress, a flexible substrate of polymer material can be introduced.

5. Fabrication feasibility of the designed sensor

In what follows, we have briefly introduced a simple strategy that could simulate the fabrication possibility of the designed magnetic fluid sensor. In fact, the experimental and fabrication procedure of many designs of PC structures have been demonstrated among the past three decades. In this regard, many different materials such as Ag, CaF_2, MgF_2, Si, SiO_2, porous Si and TiO_2 received a significant interest due to their simplicity in the experimental verifications of PC designs due to their chemical and physical characteristics including their microelectronic processing compatibility, high matching, and high surface area as well [40-42]. Therefore, many different applications including optical and sensing structures have been fabricated using these materials [29,43,44]. For our proposed sensor, CaF_2 provides high stability, low absorption coefficient, exceptional hardness, high melting point besides it can be classified as an insoluble material [45,46]. These characteristics could make it as a promising candidate for PC structures. In contrast, TiO_2 provides high refractive index, good mechanical stability besides its low thermo-optic coefficient. Then, Ag like Au has promising surface plasmon resonance properties. In addition, Ag is widely considered in many different applications including electro-optical, nanoelectronics, medical imaging, photocatalysis and nonlinear optics applications.

Now, the fabrication procedure can be simulated by the deposition of a thin Ag layer on the prism using RF sputtering technique [3]. Then, chemical vapor deposition technique can be used for the deposition of polymer layer of polyimide (PI) on the prism/Ag system [47]. Moreover, molecular beam epitaxy technique is suggested to grow the PC structure of TiO_2/CaF_2 on prism/Ag/PI [48,49]. Thus, the whole designed structure can be now configured as, [prism/Ag/PI/$(TiO_2/CaF_2)^{15}$]. Finally, the cavity layer can be introduced through the fabricated structure by etching the PI layer using the chemical etching method [50].

6. Conclusions

To sum up, we have introduced a simple design based on the inclusion of a cavity layer filled of NaI magnetic fluid between a thin Ag layer and a 1D PC structure to act as a highly sensitive magnetic fluid sensors. Notably, the refractive index of the analyte material provides some changes with the applying of an external weak magnetic field. The numerical findings are essentially dependent on the emergence of a coupled Tamm/Fano resonant peak inside the reflectance spectrum. Meanwhile, the spectral properties of this resonant peak, specifically its position, is significantly sensitive to an external weak magnetic field in unit of Oe. In this regard, the position of Tamm/Fano modes shifts upward by increasing the external magnetic field. Therefore, a detailed optimi-

zation process including thickness of each layer, refractive indices, and incident angel were carried out towards the best performance of the designed sensor. The numerical investigations show that the sensor is specified with relatively high performance including a sensitivity of 1500 nm/RIU and quality factor 4394.

Author contributions statement
Project administration, F.R., M.M., H.A.E., and A.M.; Supervision, W.A., A.M.E., H.A.E., M.R.A., and A.M.; Software, F.R.; Visualization, H.A.E., M.M., F.R., A.M.; Writing – review and editing, H.A.E., M.M., and A.M.; Writing – original draft, F.R.; Methodology, A.M., A.M.E., H.A.E., and W.A., and M.R.A.; Data curation, F.R., M.M., A.M., and H.A.E. All authors have read and agreed to the published version of the manuscript.

Conflict of interest
The authors declare no conflict of interest.

Availability of data and material
Requests should be addressed to corresponding author on a reasonable request.

Funding
The authors extend their appreciation to King Saud University for funding this work through Researchers Supporting Project number (RSP2025R133), King Saud University, Riyadh, Saudi Arabia.

References

[1] Yablonovitch E., *Inhibited spontaneous emission in solid-state physics and electronics*, Physical Review Letters **58**(20), 1987: 2059. https://doi.org/10.1103/PhysRevLett.58.2059
[2] John S., *Strong localization of photons in certain disordered dielectric superlattices*, Physical Review Letters **58**(23), 1987: 2486. https://doi.org/10.1103/PhysRevLett.58.2486
[3] Shaban M., Ahmed A.M., Abdel-Rahman E., Hamdy H., *Tunability and sensing properties of plasmonic/1D photonic crystal*, Scientific Reports **7**, 2017: 41983. https://doi.org/10.1038/srep41983
[4] Elsayed H.A., Abadla M.M., *Transmission investigation of one-dimensional Fibonacci-based quasi-periodic photonic crystals including nanocomposite material and plasma*, Physica Scripta **95**(3), 2020: 035504. https://doi.org/10.1088/1402-4896/ab4c68
[5] Devashish D., Ojambati O.S., Hasan S.B., van der Vegt J.J.W., Vos W.L., *Three-dimensional photonic band gap cavity with finite support: Enhanced energy density and optical absorption*, Physical Review B **99**(7), 2019: 075112. https://doi.org/10.1103/PhysRevB.99.075112
[6] Kang P., Ogunbo S.O., Erickson D., *High resolution reversible color images on photonic crystal substrates*, Langmuir **27**(16), 2011: 9676-9680. https://doi.org/10.1021/la201973b
[7] Joannopoulos J., Meade R.D., Winn J., *Photonic Crystals–Princeton*, Princeton University Press, NJ, 1995.
[8] González L.E., Ordoñez J.E., Zambrano G., Porras-Montenegro N., *$YBa_2Cu_3O_{7-x}/BaTiO_3$ 1D superconducting photonic crystal with tunable broadband response in the visible range*, Journal of Superconductivity and Novel Magnetism **31**(7), 2018: 2003-2009. https://doi.org/10.1007/s10948-017-4427-4
[9] Chen M.-S., Wu C.-J., Yang T.-J., *Optical properties of a superconducting annular periodic multilayer structure*, Solid State Communications **149**(43-44), 2009: 1888-1893. https://doi.org/10.1016/j.ssc.2009.08.002
[10] Thapa K.B., Srivastava S., Tiwari S., *Enlarged photonic band gap in heterostructure of metallic photonic and superconducting photonic crystals*, Journal of Superconductivity and Novel Magnetism **23**, 2010: 517-525. https://doi.org/10.1007/s10948-010-0644-9

[11] Segovia-Chaves F., Vinck-Posada H., *Tuning of transmittance spectrum in a one-dimensional superconductor-semiconductor photonic crystal*, Physica B: Condensed Matter **543**, 2018: 7-13. https://doi.org/10.1016/j.physb.2018.05.005

[12] Malek C., Aly A.H., Alamri S., Sabra W., *Tunable PBGs with a cutoff frequency feature in Fibonacci quasi-periodic designs containing a superconductor material at THz region*, Physica Scripta **96**(10), 2021: 105501. https://doi.org/10.1088/1402-4896/ac0275

[13] Saito A., Shirakawa M., Kitamura K., Noguchi Y., Mukaida M., Yamasaki H., Nakagawa Y., Ohshima S., *Dependence of surface resistance in HTS thin films on a DC magnetic field*, IEEE Transactions on Applied Superconductivity **15**(2), 2005: 3692-3695. https://doi.org/10.1109/TASC.2005.849394

[14] Herrera A.Y., Calero J.M., Porras-Montenegro N., *Pressure, temperature, and thickness dependence of transmittance in a 1D superconductor-semiconductor photonic crystal*, Journal of Applied Physics **123**(3), 2018: 033101. https://doi.org/10.1063/1.5009708

[15] Trabelsi Y., *Tunable properties of omnidirectional band gap based on photonic quasicrystals containing superconducting material*, Optical and Quantum Electronics **53**, 2021: 76. https://doi.org/10.1007/s11082-020-02708-8

[16] Mohamed M.S., Hameed M.F.O., El-Okr M.M., Obayya S.S.A., *Characterization of one dimensional liquid crystal photonic crystal structure*, Optik **127**(20), 2016: 8774-8781. https://doi.org/10.1016/j.ijleo.2016.06.101

[17] Zhang H.-F., Liu S.-B., Kong X.-K., Bian B.-R., Ma B., *Enhancement of omnidirectional photonic bandgaps in one-dimensional superconductor–dielectric photonic crystals with a staggered structure*, Journal of Superconductivity and Novel Magnetism **26**, 2013: 77-85. https://doi.org/10.1007/s10948-012-1712-0

[18] Goyal A.K., Dutta H.S., Pal S., *Recent advances and progress in photonic crystal-based gas sensors*, Journal of Physics D: Applied Physics **50**(20), 2017: 203001. https://doi.org/10.1088/1361-6463/aa68d3

[19] Gandhi S., Awasthi S.K., Aly A.H., *Biophotonic sensor design using a 1D defective annular photonic crystal for the detection of creatinine concentration in blood serum*, RSC Advances **11**, 2021: 26655-26665. https://doi.org/10.1039/D1RA04166E

[20] Kumar S., Das R., *Refractive index sensing using a light trapping cavity: A theoretical study*, Journal of Applied Physics **123**(23), 2018: 233103. https://doi.org/10.1063/1.5029233

[21] El-Ghany S.E.-S. Abd, *Temperature sensors based on one dimensional photonic crystals with different double defects*, Journal of Nanoelectronics and Optoelectronics **13**(2), 2018: 221-228. https://doi.org/10.1166/jno.2018.2199

[22] Sang Z.-F., Li Z.-Y., *Properties of defect modes in one-dimensional photonic crystals containing a graded defect layer*, Optics Communications **273**(1), 2007: 162-166. https://doi.org/10.1016/j.optcom.2006.12.008

[23] Kriegel I., Scotognella F., *Photo-thermal effect with photonic crystals for photocatalysis and water desalination*, Optical Materials: X **16**, 2022: 100215. https://doi.org/10.1016/j.omx.2022.100215

[24] Juneau-Fecteau A., Fréchette L.G., *Tamm plasmon-polaritons in a metal coated porous silicon photonic crystal*, Optical Materials Express **8**(9), 2018: 2774-2781. https://doi.org/10.1364/OME.8.002774

[25] Tamm I.E., *O vozmozhnoi sviazi elektronov na poverkhnostiakh kristalla*, Zh. Eksp. Teor. Fiz **3**(1), 1933: 34-35.

[26] Zayats A.V., Smolyaninov I.I., *Near-field photonics: Surface plasmon polaritons and localized surface plasmons*, Journal of Optics A: Pure and Applied Optics **5**(4), 2003: S16. https://doi.org/10.1088/1464-4258/5/4/353

[27] Almawgani A.H.M., Elsayed H.A., Mehaney A., Taha T.A., Alrowaili Z.A., Ali G.A., Sabra W., Asaduzzaman S., Ahmed A.M., *Photonic crystal nanostructure as a photodetector for NaCl solution monitoring: theoretical approach*, RSC Advances **13**(10), 2023: 6737-6746. https://doi.org/10.1039/D3RA00308F

[28] FANO U., *Effects of configuration interaction on intensities and phase shifts*, Physical Review **124**(6), 1961: 1866. https://doi.org/10.1103/PhysRev.124.1866

[29] WANG Z., WANG C., SUN F., FU Z., XIAO Z., WANG J., TIAN H., *Double-layer Fano resonance photonic-crystal-slab-based sensor for label-free detection of different size analytes*, Journal of the Optical Society of America B **36**(2), 2019: 215-222. https://doi.org/10.1364/JOSAB.36.000215

[30] AHMED A.M., MEHANEY A., *Ultra-high sensitive 1D porous silicon photonic crystal sensor based on the coupling of Tamm/Fano resonances in the mid-infrared region*, Scientific Reports **9**, 2019: 6973. https://doi.org/10.1038/s41598-019-43440-y

[31] FAN P., YU Z., FAN S., BRONGERSMA M.L., *Optical Fano resonance of an individual semiconductor nanostructure*, Nature Materials **13**, 2014: 471-475. https://doi.org/10.1038/nmat3927

[32] DREGELY D., NEUBRECH F., DUAN H., VOGELGESANG R., GIESSEN H., *Vibrational near-field mapping of planar and buried three-dimensional plasmonic nanostructures*, Nature Communications **4**, 2013: 2237. https://doi.org/10.1038/ncomms3237

[33] PERSHAN P.S., *Magneto-optical effects*, Journal of Applied Physics **38**(3), 1967: 1482-1490. https://doi.org/10.1063/1.1709678

[34] YING Y., HU N., SI G., XU K., LIU N., ZHAO J.-Z., *Magnetic field and temperature sensor based on D-shaped photonic crystal fiber*, Optik **176**, 2019: 309-314. https://doi.org/10.1016/j.ijleo.2018.09.107

[35] ALY A.H., ELSAYED H.A., AMEEN A.A., MOHAMED S.H., *Tunable properties of one-dimensional photonic crystals that incorporate a defect layer of a magnetized plasma*, International Journal of Modern Physics B **31**(31), 2017: 1750239. https://doi.org/10.1142/S0217979217502393

[36] ELSAYED H.A., *A multi-channel optical filter by means of one dimensional n doped semiconductor dielectric photonic crystals*, Materials Chemistry and Physics **216**, 2018: 191-196. https://doi.org/10.1016/j.matchemphys.2018.06.016

[37] ELSAYED H.A., *Quasiperiodic photonic crystals for filtering purpose by means of the n doped semiconductor material*, Physica Scripta **95**(6), 2020: 065504. https://doi.org/10.1088/1402-4896/ab7f4a

[38] AHMED A.M., MEHANEY A., ELSAYED H.A., *Detection of toluene traces in exhaled breath by using a 1D PC as a biomarker for lung cancer diagnosis*, The European Physical Journal Plus **136**, 2021: 626. https://doi.org/10.1140/epjp/s13360-021-01621-7

[39] CHEN Y.F., YANG S.-Y., TSE W.S., HORNG H.E., HONG C.-Y., YANG H.C., *Thermal effect on the field -dependent refractive index of the magnetic fluid film*, Applied Physics Letters **82**(20), 2003: 3481 -3483. https://doi.org/10.1063/1.1576292

[40] SALEM M.S., SAILOR M.J., HARRAZ F.A., SAKKA T., OGATA Y.H., *Electrochemical stabilization of porous silicon multilayers for sensing various chemical compounds*, Journal of Applied Physics **100**(8), 2006: 083520. https://doi.org/10.1063/1.2360389

[41] ZHANG H., LIN L., LIU D., CHEN Q., WU J., *Optical nose based on porous silicon photonic crystal infiltrated with ionic liquids*, Analytica Chimica Acta **953**, 2017: 71-78. https://doi.org/10.1016/j.aca.2016.11.053

[42] SEGURA GARCÍA D., CARDADOR D., VEGA D., SANTOS M., DIOS F., RODRIGUEZ A., *Bandgap widening in macroporous silicon photonic crystals by multiperiodic structures*, Journal of Physics Communications **2**(5), 2018: 055014. https://doi.org/10.1088/2399-6528/aac0ec

[43] CAROSELLI R., SÁNCHEZ D.M., PONCE ALCÁNTARA S., PRATS QUILEZ F., TORRIJOS MORÁN L., GARCÍA -RUPÉREZ J., *Real-time and in-flow sensing using a high sensitivity porous silicon microcavity-based sensor*, Sensors **17**(12), 2017: 2813. https://doi.org/10.3390/s17122813

[44] PHAM V.H., BUI H., NGUYEN T.V., NGUYEN T.A., PHAM T.S., PHAM V.D., TRAN T.C., HOANG T.T., NGO Q.M., *Progress in the research and development of photonic structure devices*, Advances in Natural Sciences: Nanoscience and Nanotechnology **7**(1), 2016: 015003. https://doi.org/10.1088/2043-6262/7/1/015003

[45] CHEN J., ZHANG Z., GUO Y., ROBERTSON J., *Electronic properties of CaF_2 bulk and interfaces*, Journal of Applied Physics **131**(21), 2022: 215302. https://doi.org/10.1063/5.0087914

[46] Baskurt M., Kang J., Sahin H., *Octahedrally coordinated single layered CaF_2: robust insulating behaviour*, Physical Chemistry Chemical Physics **22**(5), 2020: 2949-2954. https://doi.org/10.1039/C9CP06015D

[47] González J.P.-P., Lamure A., Senocq F., *Polyimide (PI) films by chemical vapor deposition (CVD): Novel design, experiments and characterization*, Surface and Coatings Technology **201**(22-23), 2007: 9437-9441. https://doi.org/10.1016/j.surfcoat.2007.05.029

[48] Nassiopoulou A.G., Tsakiri V., Ioannou-Sougleridis V., Photopoulos P., Menard S., Bassani F., d'Avitaya F.A., *Light-emitting structures based on nanocrystalline (Si/CaF_2) multiquantum wells*, Journal of Luminescence **80**(1-4), 1998: 81-89. https://doi.org/10.1016/S0022-2313(98)00073-8

[49] Ioannou-Sougleridis V., Ouisse T., Nassiopoulou A.G., Bassani F., d'Avitaya F.A., *Nonlinear electrical transport in nc-Si/CaF_2 multilayer structures with ultrathin CaF_2 layers*, Journal of Applied Physics **89**(1), 2001: 610-614. https://doi.org/10.1063/1.1330551

[50] Ejima T., Ouchi K., Watanabe M., *Si–K absorption spectra of Si/CaF_2 and Si/LiF multilayers*, Journal of Electron Spectroscopy and Related Phenomena **101-103**, 1999: 833-838. https://doi.org/10.1016/S0368-2048(98)00433-2

Received February 17, 2025
in revised form March 17, 2025